

Temperature controlled tensile testing of individual nanowires

Lisa Y. Chen,¹ Soraya Terrab,^{1,2} Kathryn F. Murphy,¹ John P. Sullivan,³ Xuemei Cheng,^{1,2} and Daniel S. Gianola^{1,a)}

(Received 16 September 2013; accepted 13 December 2013; published online 8 January 2014)

We present a novel experimental method for quantitatively characterizing the temperature-dependent mechanical behavior of individual nanostructures during uniaxial straining. By combining a microelectromechanical tensile testing device with a low thermal mass and digital image correlation providing nm-level displacement resolution, we show successful incorporation of a testing platform in a vacuum cryostat system with an integrated heater and temperature control. Characterization of the local sample temperature and time-dependent response at both low and high temperature demonstrates a testing range of ~90–475 K and steady-state drift rates less than 0.04 K/min. *In situ* operation of the tensile testing device employing resistively heated thermal actuators while imaging with an optical microscope enables high-resolution displacement measurements, from which stress-strain behavior of the nanoscale specimens is deduced. We demonstrate the efficacy of our approach in measuring the temperature dependence of tensile strength in nominally defect-free (110) Pd nanowhiskers. We uncover a pronounced sensitivity of the plastic response to testing temperature over a range of ~300 K, with an ultimate strength in excess of 6 GPa at low temperature. The results are discussed in the context of thermally activated deformation mechanisms and defect nucleation in defect-free metallic nanostructures. © 2014 AIP Publishing LLC. [http://dx.doi.org/10.1063/1.4858815]

I. INTRODUCTION AND BACKGROUND

Successful design and implementation of devices based on nanoscale materials requires understanding of the deformation mechanisms of their building block components. While the superior strength and elastic deformation range in nanoscale elements such as nanowires and thin films are promising for their application as flexible electrodes, 1,2 sensors, 3 and resonators, 4,5 their mechanical response cannot be directly extrapolated from bulk material behavior. In nanoscale applications based on non-mechanical material properties such as surface plasmon resonance in metallic nanostructures 1,6,7 or thermal conductivity, 8,9 predictable functionality often hinges on the mechanical integrity of individual components, as large stresses that may approach or exceed the material failure limit are incurred during fabrication and operation.

For many applications, the coupling of temperature and stress in governing response is inevitable due to large temperature ranges of the operational environments. ^{10–23} Even within modest temperature ranges, the influence of temperature on material phenomena is strongly enhanced by size. High surface-to-volume ratios can lead to surface diffusion-driven melting below bulk melting temperature. ^{24–26} In addition, whereas in bulk metals plastic deformation is largely driven by pre-existing dislocation interactions, dislocations often need to be nucleated near the theoretical strength in pristine single-crystal nanostructures, a process that is believed to be thermally activated. ^{27–29} Moreover, the observed behavior

Accordingly, several testing methods have been developed to investigate temperature-dependent mechanical behavior in small volumes. Temperature control has been integrated with microscale compression^{33–35} and bending³⁶ setups to characterize pillar and cantilever structures, respectively. Hot nanoindentation has also been developed for probing submicron-sized volumes in coatings and thin films.^{37–45} However, interpretation of results from such testing modalities often involves assumptions about testing geometry and substrate effects, and temperatures are limited to above room temperature. Tensile testing can provide truly uniaxial deformation with fewer constraints on sample geometry, from which the full suite of mechanical behavior can be directly obtained. 1,3,46 Tensile testing of thin films has been integrated with low temperatures to circumvent issues related to specimen thermal stability, 47,48 but currently no setup to our knowledge has been applied to testing nanowire or nanotube geometries.

Whereas several testing methods for such small geometries have been developed for *in situ* imaging platforms, 1, 2, 49–53 temperature control is not easily incorporated in large part because of the large thermal masses of testing components. MEMS platforms 5, 13, 54 are particularly versatile due to their small footprint and can easily be transported with a prepared sample to other operating environments. In

¹Department of Materials Science and Engineering, University of Pennsylvania, Philadelphia, Pennsylvania 19104, USA

²Department of Physics, Bryn Mawr College, Bryn Mawr, Pennsylvania 19010, USA

³Sandia National Laboratories, Livermore, California 94550, USA

following incipient plasticity often differs greatly from what is observed in bulk, and the physical origins of these processes are still being investigated.^{30–32} Taken as a whole, a regime of behavior characterized by extreme stresses and pronounced temperature dependencies is expected in defect-free nanostructures but has yet to be explored experimentally.

a)Email: gianola@seas.upenn.edu

particular, the low thermal mass of MEMS stages is favorable for exploring temperature-dependent material properties above, as well as below, room temperature.

This paper details a novel nanoscale tensile testing methodology for determining temperature-dependent mechanical behavior of individual nanowires over a range of 90-475 K. Our paper begins by describing the materials and MEMS tensile testing platform, followed by integration into a cryostat system. We describe characterization of the device operation at various temperatures, and outline a typical procedure for non-ambient testing. We then demonstrate the efficacy of our approach as applied to tensile testing of (110) Pd nanowhiskers (NWs) – nominally defect-free single crystalline nanowires – over a wide range of temperatures, which exhibit strongly temperature-sensitive deformation and fracture strengths near the theoretical limit of strength of a crystal. The Concluding Remarks discuss the advantages of our testing methodology and propose several possible improvements to the system.

II. EXPERIMENTAL

A. Materials and specimens

The single-crystalline Pd NWs examined in this study were grown by thermal evaporation onto [0001]-SrTiO $_3$ or [0001]-Al $_2$ O $_3$ substrates under ultra-high vacuum conditions. The NWs were determined to be axially oriented along the $\langle 110 \rangle$ direction by electron diffraction analysis on at least ten NWs from each substrate, and possess high aspect-ratios, with lengths 5 < l < 20 μ m and diameters 30 < d < 150 nm. The substrates are maintained at elevated temperatures of 950 °C to promote diffusion of Pd atoms along the surface. Substrate surface features such as atomic steps act as nucleation sites

for growth, and the high interfacial energy leads to the growth of islands and whiskers instead of a conformal film. The near-equilibrium growth conditions result in NWs free of visible defects with fracture strengths in the range of the theoretical strength.^{2,32,54} Further details of the fabrication process can be found in Refs. 2 and 55.

B. MEMS testing device and vacuum cryostat system

Individual NWs were harvested in a scanning electron microscope (SEM) with a Kleindiek nanomanipulator equipped with a tungsten probe, then aligned and mounted to a MEMS tensile testing stage (Fig. 1(c)). Since most of the wires are smaller in diameter than the radius of the probe tip used for manipulation (>100 nm), trenches were etched into the Si grips near the edges during preparation using a focused-ion beam (Fig. 1(c)) to ensure that the mounted NW is flush with the grip surface. The NWs were secured across the Si grips using electron beam induced deposition (EBID) of a Pt-containing hydrocarbon matrix. Actuation of the testing device was achieved by Joule heating and corresponding thermal expansion of polysilicon chevron beams (Fig. 1(c)). A SiN_x strip fabricated on the actuator-side grip mitigated heat flow to the specimen during testing. Force on the specimen was measured by the displacement of the load cell, which consists of a compound flexure beam system with a stiffness of 44 N/m.

The entire MEMS stage was mounted and wire bonded to a ceramic dual-inline package (Fig. 1(b)). Due to the low thermal mass of the package and stage, a non-ambient temperature testing setup employing a Janis ST-500 microscopy cryostat was used to uniformly heat or cool the stage. The cryostat consists of a sealed vacuum chamber with

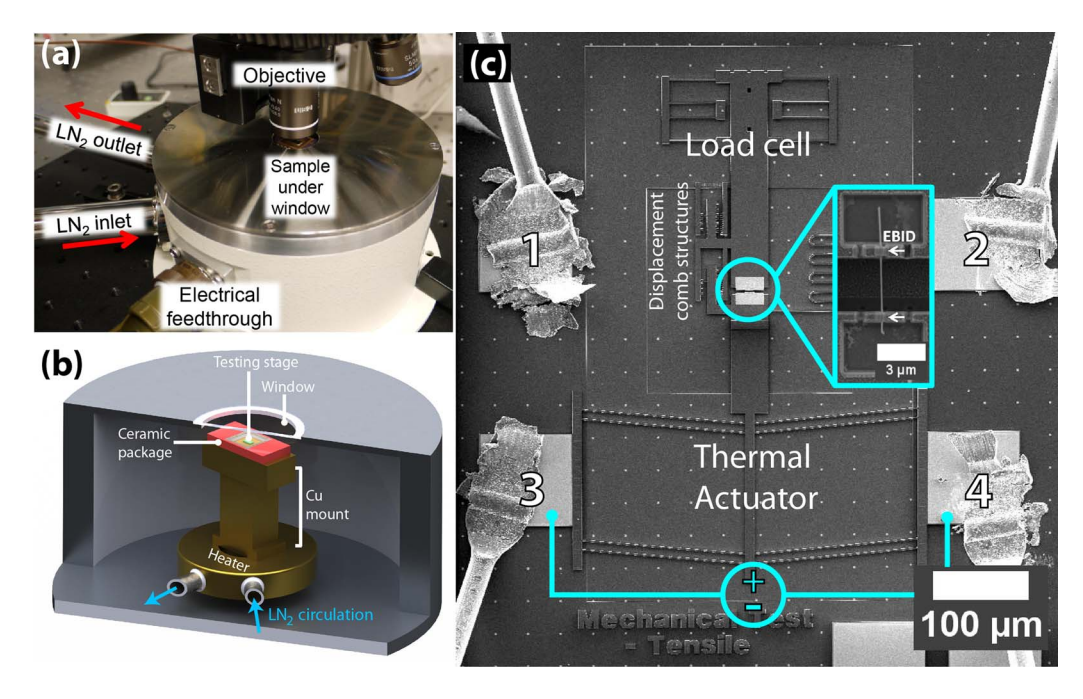


FIG. 1. (a) Photograph of the vacuum cryostat setup under the optical microscope. (b) Schematic of the inner chamber. Temperature sensors (not shown) are located at the top of the testing stage, on the Cu mount, and at the heater. (c) SEM micrograph of the MEMS-based tensile testing stage. Inset shows a zoom of the grips after attaching a Pd NW specimen using Pt-containing EBID. Wire bonds 1 and 2 are used for grounding the stage during SEM imaging. Wire bonds 3 and 4 are the electrical connections for actuating the chip.

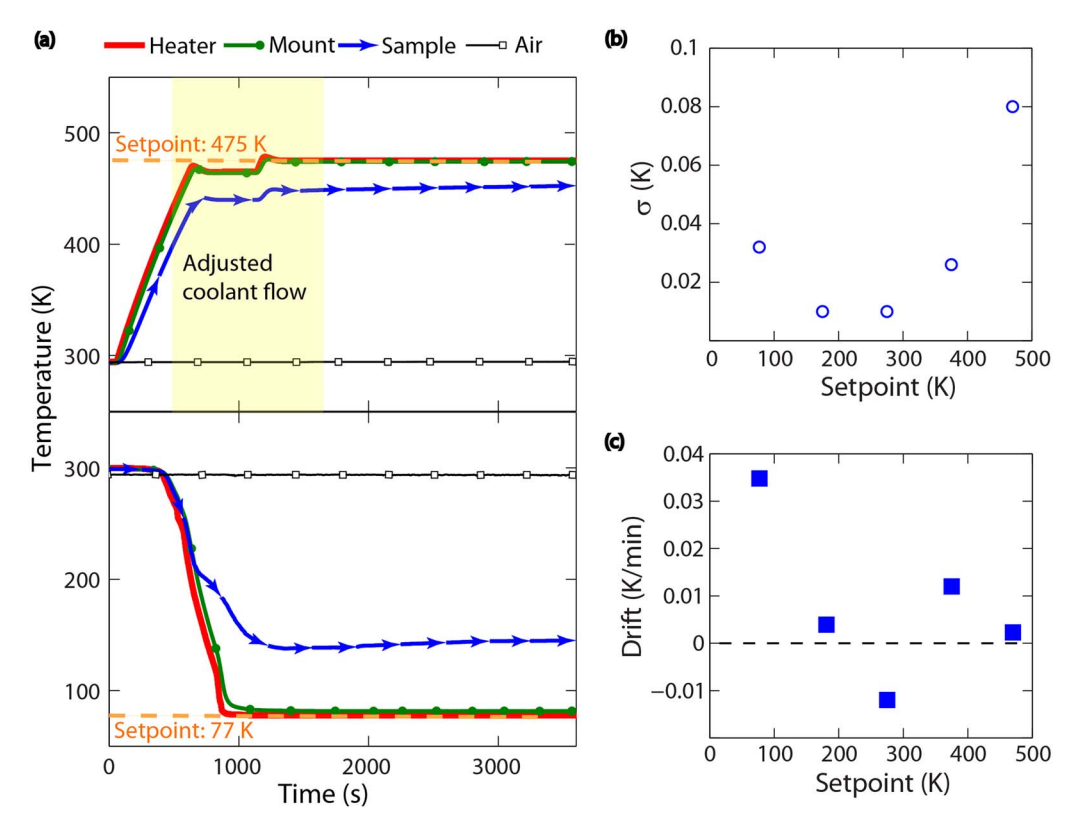


FIG. 2. (a) Time dependence of temperature of the thermoresistive heater, copper mount, sample, and laboratory air when heating to a setpoint value of 475 K (top) and during liquid nitrogen cooling (77 K) (bottom). (b) Temperature noise at the sample, measured as the standard deviation σ of a 1000-s time interval after a steady-state temperature is reached. (c) Temperature drift at the sample during the 1000-s interval.

a fused silica window in the top flange for imaging the stage (Fig. 1(a)). The cryostat was continuously pumped using a HiCube 80 Eco turbo pumping station (Pfeiffer Vacuum) down to pressures as low as 10^{-6} mbar. Liquid nitrogen (LN₂) entered from the inlet leg via a transfer hose, ran a path directly connected to the mount and heater, and exited through the outlet leg. Each leg is a pair of coaxial pipes, where the outer pipe is isolated from the inner pipe by vacuum to promote the continuous flow of nitrogen in liquid form until it reaches the exhaust in its gaseous state as well as to minimize condensation.

The chamber interior consists of a Cu mount directly coupling the sample to the cryogen path and a thermoresistive coil heater at the bottom (Fig. 1(b)). The mount includes clamps with copper wires to mechanically secure and electrically connect the ceramic package. Thermal pastes rated for cryogenic and high temperatures were used to further promote conduction between the mount and the sample. The wiring on the mount clamps is connected to electrical feedthroughs that enable the operation of the actuator by an externally connected power supply. Temperature sensor feedthroughs enable measurements of temperature at different points within the cryostat. Three temperature sensors were used inside the chamber: a thermocouple adhered with silver paint to the top of the testing stage substrate; a thermocouple on the mount midway between the cryogen path and sample; and a Si diode sensor at the foot of the mount on the resistive heater that provides feedback to a proportional-integral-derivative (PID) temperature controller. The different temperature measurements are referred to here as the sample temperature (T_S) , mount temperature (T_M) , and heater temperature (T_H) .

The heater temperature was determined by the cryogen flow and the temperature control parameters, with control feedback enabled at this location by the PID loop. The sample temperature, however, was governed by additional factors and may be significantly different from the setpoint. With the chamber constantly being pumped at high vacuum, convection from the chamber walls is negligible. Due to the close proximity of the top of the ceramic package to the top flange and window (<0.5 mm), radiation can, in contrast, be significant and lead to excessive heating of the sample during cooling. Even with thermal paste applied to the bottom of the ceramic package, the sample temperature can be over 100 K away from the setpoint owing to radiation as discussed below. This large difference between the sample and heater underscores the importance of measuring temperature at multiple points, especially at or near the sample. The system used here is capable of achieving a nominal temperature range at the heater of 77–475 K. We note that this temperature range was selected to avoid high-temperature regimes where nanoscale instabilities have been reported to appear. 24,26

C. Achieving and controlling sample temperature

At a pressure of 10^{-6} mbar, continuous cryogen (LN₂) flow enabled the heater block to achieve steady state at 77 K within 500 s of opening the dewar valve. For elevated temperature tests, both thermoresistive coil heating and active

cooling were necessary for temperature control. In addition to the PID temperature controller, the flow of LN_2 , or an alternative cooling fluid such as N_2 gas, provided a stable cold reference temperature. As shown in the top panel in Fig. 2(a), the flow rate control of the coolant affected the temperature stability, which can be attained upon adjusting the flow properly. Once steady state was attained, noise in the temperature reading at the sample (calculated as the standard deviation of a 1000-s time interval) reached a maximum of 0.08 K at a setpoint of 475 K and a value of 0.035 K at 77 K.

Temperature drift at different setpoints has also been characterized to estimate the overall change in temperature during testing. The drift ranges from a maximum value at 77 K of 0.035 K/min to a minimum at 475 K of 0.002 K/min. For a typical nanomechanical tensile test of 20 min, the highest drift value at the 77 K setpoint temperature provides an upper bound for an average temperature change of 0.7 K.

Fig. 3 shows the sample-to-heater and mount-to-heater temperature differences, measured at five setpoint temperatures with the use of a radiation shield. At the lowest setpoint temperature, the mount-to-heater temperature difference was 4.08 K, whereas the temperature difference between the sample and heater was as high as 67.0 K. At the high-temperature target of 475 K the differences are smaller, with temperature offsets at the mount and sample of 0.9 K and 23.4 K, respectively. Nevertheless, a stable steady-state temperature at the sample was attained during both heating and cooling cycles, although the experimental temperature differences along the thermal path from heater to sample signify the importance of additional heat transfer mechanisms. Namely, the vacuum environment in the cryostat eliminates convective and air conduction heat losses from the chamber, but thermal radiation and solid conduction losses remain. Radiation played an important factor in the measured temperature offset due to the large temperature difference between the cryostat and the laboratory and the close proximity of the sample to the top flange and window. At low temperature, infrared radiation emitted from the cryostat chamber walls was partially absorbed by the sample and its surroundings, while at high temperature

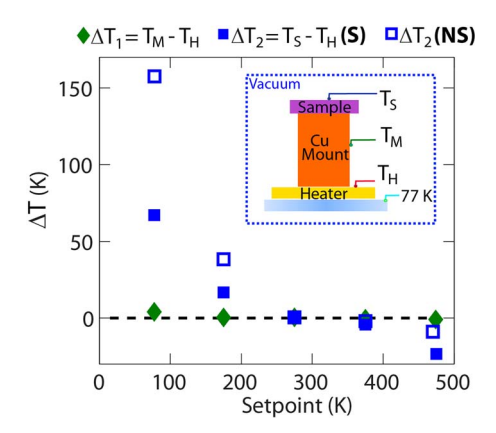


FIG. 3. Temperature difference between copper mount and heater, ΔT_1 , and sample and heater ΔT_2 . The latter includes measurements both with a radiation shield (S) and without (NS, open squares). The inset is a schematic of the cryostat cross-section showing the connected temperature sensors (top to bottom) at the sample, copper mount, and heater. The liquid nitrogen flow path is at the base of the cryostat.

the sample lost heat via radiative losses. To verify if radiation, resulting from a temperature gradient in the system, was the dominant source of thermal loss, a Peltier module was placed near the cryostat window to cool the window during LN_2 flow into the cryostat. A decrease in sample temperature confirmed that radiation is a main source for temperature offset.

In order to reach low temperature offsets at the sample, solutions to reduce the influence of thermal radiation at low setpoint temperatures were implemented. An aluminum radiation shield on the ceramic package was hence introduced to reflect radiation incident from the surroundings. The shield was cut from a sheet of aluminum foil and secured to the top of the ceramic package with Kapton tape. An aperture was cut in the middle of the foil to allow viewing of the testing stage as well as preventing contact between the foil and the wire bonds. During LN₂ cooling down to 77 K, the temperature difference between the sample and heater was reduced by as much as 90 K with the presence of the radiation shield. In general, the shield provides optimal conditions for testing particularly at setpoints below room temperature.

Since the specimen to be tested was mounted on polysilicon grips suspended above the testing stage substrate, it is worth commenting on heat transfer mechanisms to the suspended specimen being tested. In order to determine the temperature difference between the substrate and the grips, a package containing a device without a clamped nanowire was mounted on a Peltier heating stage under a confocal Raman microscope (Fig. 4). Raman spectra were obtained in air at room and elevated temperatures from both the device grips and substrate. The frequency of the strongest peak in the Si Raman spectrum displays a linear dependence on temperature near room temperature, 56,57 and this dependence was used to measure temperature rise as the setpoint was increased (Fig. 4). Substrate temperatures measured between 295 K to 383 K agreed well with the temperature measured at the grip, with any differences being within the uncertainty of the Raman measurement (\sim 3 K). We attribute this efficient heat transfer primarily to solid conduction through polysilicon and air conduction across a gap of about 2 μ m from the substrate, overwhelming the expected heat loss to the surrounding air environment. These mechanisms are consistent with

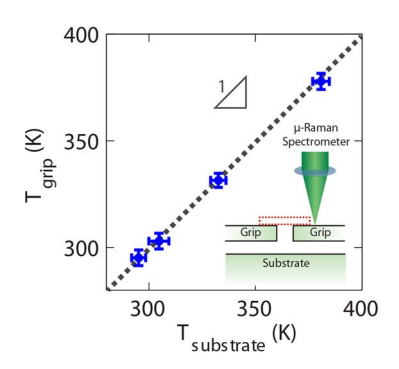


FIG. 4. Raman thermography measurements of the substrate ($T_{substrate}$) and grip (T_{grip}) temperatures. Error bars represent the standard deviation of 20 measurements. The dotted line has a slope of 1, corresponding to thermal equilibrium between the substrate and the specimen grips. The inset is a schematic of the temperature measurement setup under the Raman objective. The dotted outline indicates where a Pd NW would be placed.

other reports of dominant heat transfer mechanisms in MEMS structures. ^{58,59} In vacuum, in the absence of air conduction from the substrate, it is expected that conduction through the polysilicon will still enable the grips to stabilize at the substrate temperature within the stabilization timeframe.

D. In situ operation and digital image correlation

1. Imaging characteristics and measurement noise floors

Load and strain on the specimen were determined by optically tracking the motion of comb structures directly attached to the grips and substrate of the MEMS device (Fig. 1(c)). The displacement of and force on the nanowire were provided by the displacements of the actuator and load cell, respectively. The difference between these displacement values normalized by the specimen gage section provided a measurement of the nominal specimen strain. The in-plane drift of the entire chip was determined and corrected for by tracking the motion of combs anchored to the substrate. Compensation for out-of-plane drift is discussed in Sec. II D 2.

During testing, images were taken at regular intervals and then processed using digital image correlation (DIC) to track the displacement of these features. A base image was divided into sub-images around high-contrast features (e.g., comb finger edges, marked by green points in Fig. 5), and the positions of these sub-images were updated for each subsequent capture based on maximization of a correlation function providing the best mapping between reference and deformed states. As the tracked structures were moving in a rigid body fashion, the correlation function was adequately determined via translations of the sub-images. Using optical imaging in the current setup, we achieved sub-pixel displacement noise floors with typical values of approximately 0.05 pixels.

The use of conventional infinity-corrected objectives (Olympus SLMPLN-N 100×) in air can produce clear images of the comb structures with high contrast at the edges requisite for precise DIC (Fig. 5). The degree of contrast can be quantified by examining histograms of gray-scale values (averaged RGB values at each pixel) for each image; for the first configuration there are both a large range and a bipolar distribution representative of the light-dark contrast at the comb finger edges. However, the presence of glass between the objective and sample introduces spherical aberrations: instead of incoming light focusing on a single plane, the focal plane is "spread" along the optical axis, resulting in blurred features and lower contrast. This is evinced in the collapsed gray value histogram and the fewer sub-image points on only the inner side of the comb features that have been used successfully for correlating images captured under this condition. To compensate for the aberrations from the window, an adjustable multi-lens, aberration-correcting objective (Olympus LUCPLFLN 40×) was successfully employed to recover the high contrast of the window-less setup. The combination of aberration correction and sub-pixel correlation resolution led to peak-to-peak displacement noise below 100 nm, as described below.

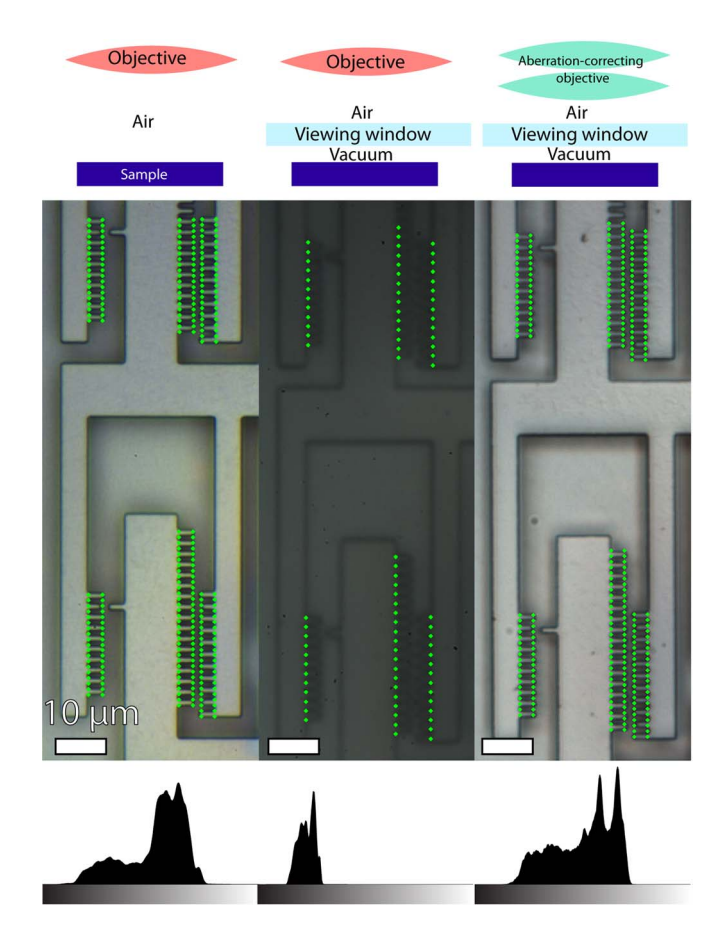


FIG. 5. Comparison of image contrast for three imaging configuration: from top to bottom, schematics of each imaging setup, optical micrographs showing the comb structures on the tensile testing device as obtained from each setup, and their respective gray value histograms. The gradient bar under each histogram represents averaged RGB values from 0 (black) to 255 (white). The green points overlaid on each micrograph are the sub-image centers used for digital image correlation (DIC) displacement tracking.

The displacement noise floors at different temperatures reflect the various sources of vibrational noise acting on the cryostat, as shown in Fig. 6. At room temperature, only the vacuum pump was constantly running and the peak-to-peak displacement noise is at a minimum of 25 nm. The addition of constant cryogen flow at 77 K increased the noise slightly. To operate at elevated temperatures, either LN₂ or N₂ gas must circulate through the cryostat to actively compensate for any overshoot by the heater; in addition, the heater power operates intermittently in response to the PID feedback loop. These factors resulted in larger noise in the displacement measurement with a maximum peak-to-peak value of 62 nm at 470 K. Both peak-to-peak and standard deviation values in nanometer and pixel units are reported in Table I and plotted as a function of setpoint temperature in Fig. 6(b).

2. Effects of drift along the optical axis

Drift may occur along the optical axis (z-direction) during temperature ramping and tensile testing and is compensated using a closed-loop piezoelectric objective scanner with a range of 200 μ m and a resolution of 1 nm. As off-focus imaging can skew relative displacement measurements

TABLE I. Measurements of	of in-plane displacemen	t noise at various	setpoint	temperatures.	All data	reported
below were measured from 1	50 sequential images.					

	Peak-to-peak		Standard deviation				
Setpoint (K)	(nm)	(pixels)	(nm)	(pixels)	Total capture time (s)	Capture interval (s)	
77	25	0.27	5	0.054	600	4	
295	25	0.27	4	0.043	300	2	
375	31	0.34	5	0.055	300	2	
470	62	0.68	11	0.119	300	2	

between the various comb features during load-unload tests and result in false displacement values, a test was conducted to quantify the artificial in-plane displacements as a consequence of the z-drift. Image sequences were taken while adjusting the objective in increments of $z = 0.2 \mu m$ (relative to the z = 0 focal plane) to an absolute displacement of 2 μ m away from focus. Using z = 0 as the base image, DIC conducted on the image sequence determined the net in-plane aberrant displacement between the anchor and actuator combs as a result of defocusing. A maximum value of 0.26 μ m inplane displacement was measured at 2 μ m off-focus. Over the course of a typical tensile test in which drift in Δz is less than $0.2 \mu m$, as indicated by the shaded region in Fig. 7, the artificial in-plane displacement reaches a maximum of 0.012 μ m. While the artificial displacement can be substantially minimized by adjusting focus during testing (i.e., this measurement represents an upper bound for drift), the measured maximum displacement of 0.012 μ m displacement remains low compared to the minimal peak-to-peak noise of $0.025 \mu m$ due to in-plane vibrations, as was shown in Fig. 6(b).

3. Calibration of thermal actuator

The amount of Joule heating in the thermal actuator chevron beams during operation of the MEMS testing device, and therefore the displacement of the actuator, is directly related to the electrical power input (P) as a function of applied current (I) and voltage (V). In case of beam degradation leading to an increase in resistance, voltage is sourced instead of current $(P = IR = V/R^2)$ to avoid catastrophic run-out of the actuator.

Actuator calibration was performed by capturing images of the testing stage at several voltage values and calculating the displacement using DIC. This information was used to linearize the voltage displacement function for different testing conditions, enabling constant displacement rates. Fig. 8 shows that stage operation in air requires higher voltages to reach displacements comparable to those achieved in vacuum due to conductive heat loss through air. In vacuum, calibration has been performed in the cryostat at various setpoint temperatures, the extremes of which are shown in Fig. 8. Several properties of Si and their temperature dependencies can

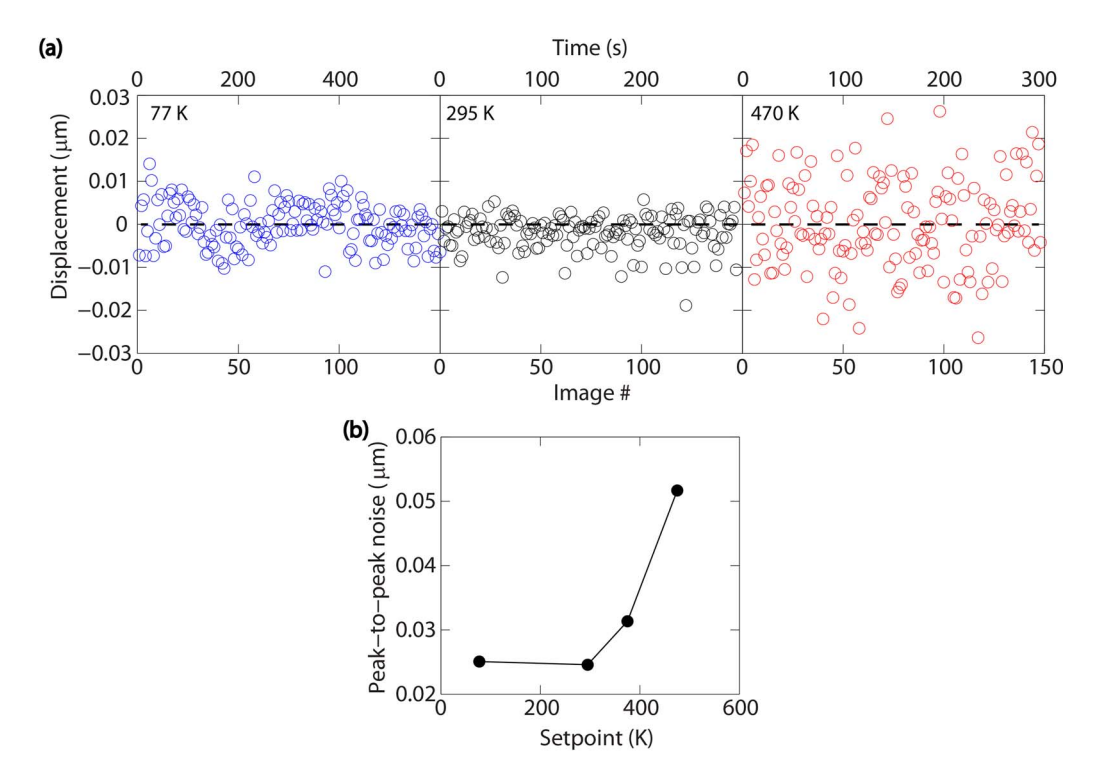


FIG. 6. (a) Time-dependent displacement values measured for a stationary setup, representing the noise for each testing temperature. Noise is the lowest at 295 K due to the absence of cryogen or coolant flow and heating. (b) Peak-to-peak displacement noise measured at different setpoint temperatures.

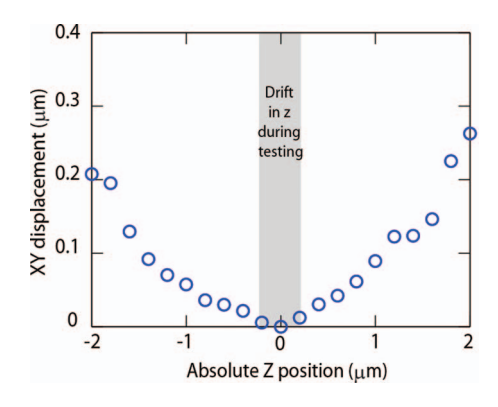


FIG. 7. (a) Artificial in-plane (XY) displacement due to drift from z-focus, measured as the absolute position relative to focus at z=0. The shaded region, indicating a $\pm 0.2~\mu m$ range in z-drift typical for an average test, corresponds to a maximum in-plane displacement of 12 nm.

affect the resulting actuator displacement induced by Joule heating. A figure of merit directly related to the Joule heating induced displacement $(\delta \propto \alpha C_p/\rho)$ can be derived by accounting for the temperature dependence of the linear coefficient of thermal expansion α , the specific heat capacity C_p , and beam resistivity ρ . ^{63–66} Plotting the figure of merit alongside the measured resistivity at low voltage (inset of Fig. 8) shows that the changes in material properties dominate the temperature-dependent actuator response. Whereas ρ alone increases with temperature and thus would reduce the power supplied to the beams $(P \propto V^2/\rho)$, the ultimate beam displacement δ response is predominately governed by the temperature dependences of α and C_p ($\delta \propto \alpha C_p/\rho$). Indeed, the actuator calibration at the highest testing temperature yielded the largest displacements for the given voltage range. We note that the crossover at high voltages between the roomtemperature (295 K) and low-temperature (144 K) calibration curves shown in Fig. 8 can be attributed to changes in the heating profiles of the thermal actuation beams during Joule heating at cryogenic temperatures, which is not accounted for in the simple figure of merit.

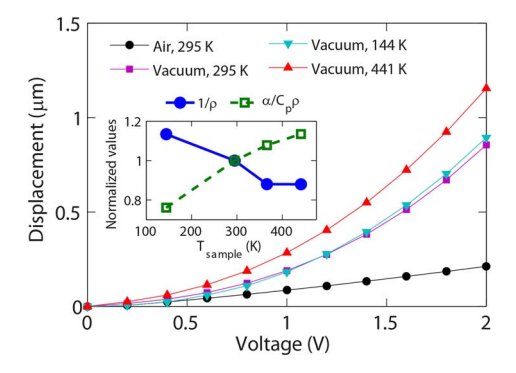


FIG. 8. Calibration curves for the displacement of the thermal actuator along the tensile axis. In vacuum, the absence of convective heating losses results in larger displacements for the same voltages compared to operation in air. The inset shows that while the resistivity of the beams increases with temperature, the thermophysical properties of the actuator materials manifest in greater lengthening of the chevron beams, and hence larger displacements, at elevated temperatures.

E. Experimental procedure

In this section, we describe the basic procedures for manipulating an individual nanowire, achieving the desired testing temperature and performing the testing, as well as the analysis necessary for deducing the full constitutive response of the tested nanomaterial.

1. Nanowire harvesting and manipulation

Individual Pd NWs were directly harvested in a SEM from their substrate and mounted across the testing stage grips using Pt-EBID.^{67,68} The NW specimens suitable for tensile testing typically grow off the edge of the substrates roughly parallel to the substrate top and bottom faces, such that tilting of the testing stage or specimen is not necessary for alignment.

Load-unload tests to stresses well below the yield point of the NWs were performed in situ in the SEM immediately after specimen mounting to verify proper operation of the MEMS device and elastic response. This testing step also enabled accurate evaluation of the elastic behavior. The apparent strain measurement from the relative displacement between the actuator and load cell grips includes EBID clamp compliance, which is a prevalent issue for accurate strain measurement. At the higher magnifications available in the SEM, rather than tracking the displacement of the comb structures, EBID contrast markers deposited in spot mode on the grips and underlying substrate were used for the apparent strain measurement (Fig. 9(b)). In comparison, the direct strain measurement was obtained by markers directly deposited on the NW and could differ significantly from the apparent strain. Several researchers have attempted to measure the properties of the organometallic materials deposited as clamps.^{69–71} Murphy et al. recently reported on contact stiffness measurements of Pt-containing EBID used for tensile testing of Pd NWs and showed that error in Young's modulus can range from 0.7% to 27%, suggesting a large influence of the clamp displacement in nominal strain measurements.⁷² While a number of strategies have been attempted to increase the stiffness of the EBID material, these researchers found the most reliable strategy for such experiments is the use of flat-clamping geometries, 72 which we have employed here.

Since the stage and specimen are cooled uniformly, it is expected that thermal contractions would pull the NW in tension during cooling, leading to a nonzero initial load on the specimen (e.g., as high as 3 GPa for diameters as small as 40 nm, provided a temperature difference $\Delta T = -150$ K). To compensate for this phenomenon, an approach was developed wherein the specimen is intentionally "pre-buckled" prior to cooling. This was achieved by supplying a fixed voltage to the actuator to increase the grip separation prior to and during mounting (Fig. 9(a)). Owing to the high aspect ratio of the nanowires, the expected critical buckling stress is less than 100 MPa, at least an order of magnitude smaller than the typical yield strength.⁵⁴ After securing the wire with EBID contacts, the voltage was ramped back down to zero, and the NW could be pulled taut during testing or during cooling. We note that this procedure is only necessary for low-temperature

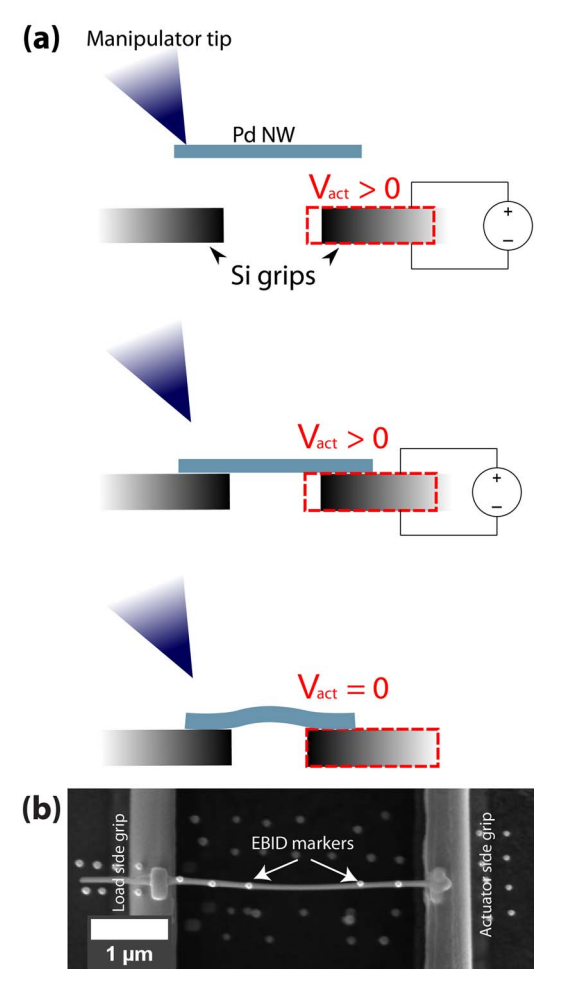


FIG. 9. (a) Schematic illustration of procedure for pre-buckling a nanowire specimen in preparation for a low-temperature test. The dotted red outline indicates the initial position of the actuator-side grip when no voltage is applied. (b) SEM micrograph of buckled Pd NW with contrast markers for *in situ* testing.

testing, as this pre-buckling effect naturally occurs during temperature ramping in preparation for high-temperature tensile testing.

2. Cooling/heating to target temperature

Prior to testing at a non-ambient setpoint temperature the ceramic package was first loaded onto the copper mount. A layer of thermal paste (either Apiezon N or Krytox for lowor high-temperature testing, respectively) was applied evenly onto both the mount surface and the bottom side of the ceramic package with a thin flat-edge. The package was then tightly clamped onto the copper mount, limiting any gap spacing between the package and the mount to ensure direct contact as well as to establish electrical connections to the MEMS device. Direct contact of the package and the mount enhanced thermal conduction for heating and cooling and additionally prevented the top of the package from touching the cryostat window. After securing the aluminum radiation shield with Kapton tape onto the ceramic package, the sample thermocouple was adhered onto the silicon chip surface with a double coating of silver paint. A piece of Kapton tape was placed to flatten the thermocouple onto the ceramic package and prevent contact with the cryostat window.

At that point, the device was ready for testing. After running a load-unload tensile test at ambient conditions to ensure chip actuation and operation, the cryostat chamber was sealed by tightly screwing the top plate. Following a roughing stage, the turbo pump was initialized to achieve vacuum. A transfer line, connecting the LN2 dewar to the cryostat inlet, was secured for subsequent cryostat cooling. The microscope objective was centered above the MEMS testing stage and the focus was adjusted approximately every 10 min. Once a pressure of $\sim 10^{-6}$ mbar was reached (typically after a few hours of pumping), an additional load-unload test at room temperature (this time under vacuum) was run to again verify chip actuation. Temperature readings from the Si diode sensor and thermocouples were recorded through a custom LabView program. Once recording was initiated, the cryostat could then be set to reach the designated setpoint.

For heating, a PID temperature controller was used to achieve and maintain the target temperature. Since a coolant was required to actively compensate in case of temperature overshoot, LN_2 flowed from the dewar and into the cryostat via the transfer line. Manual regulation of the flow of cryogen into the chamber was achieved via a valve at the transfer line.

Temperature values reported for a given experiment were calculated from the average temperature profile in the steady-state regime over the duration of a tensile test. A typical time of 1500–2500 s was needed to achieve temperature stability, as shown in Fig. 2. After steady-state temperature was reached, imaging conditions were then verified to prepare for tensile testing at the stable temperature. Tensile testing could proceed once the focus remained fixed, in order to reduce artificial in-plane displacements as discussed in Sec. II D 2. A fixed nominal strain rate was programmed and the Pd NW specimen was run through several load-unload cycles before ultimately fracturing. Low-resolution DIC was performed real-time as images were being acquired during tensile testing to monitor progress and identify when yield or fracture occurred.

III. REPRESENTATIVE RESULTS

In this section, we report the application of the previously described method to temperature-dependent tensile testing of individual Pd NWs to highlight the capabilities of our technique in the context of thermally activated plastic deformation in metallic nanostructures.

A. Load-displacement response of Pd nanowires

Using the methods described herein, we first subjected a Pd NW (d=46 nm) to load-unload cycles, and ultimately to fracture, at a constant actuator displacement rate of 3.0 nm/s (NW strain rate of approximately 1×10^{-4} s⁻¹) to determine its mechanical response at different temperatures. Fig. 10 shows measurements of the displacement evolution of the load cell (black curve), actuator (blue curve), and relative grip separation (red curve), which are used to deduce

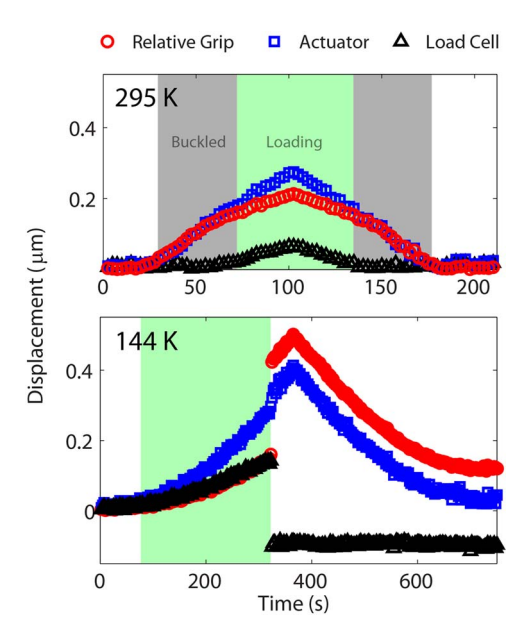


FIG. 10. Displacement measurements for tests on the same Pd NW ($d=46\,$ nm) during load-unload at room temperature (top panel) and during load-to-fracture at 144 K (bottom panel). The buckled region visible at room temperature is no longer present at low temperatures due to thermal contraction of the NW. During the load-to-fracture test, since displacements are always measured relative to the starting positions at the beginning of the test, the negative position of the load cell after fracture is the true zero-load position. This indicates a pre-tension in the NW prior to the test.

the stress-strain response of the NW. The top panel shows a load-unload cycle performed at room temperature (295 K) to confirm proper operation of the device before cooling experiments. A few regimes of behavior can be discerned from the load-unload response. Upon initial motion of the actuator (denoted by gray shaded region), the load was initially sluggish to response, which is ascribed to a slightly pre-buckled state of the NW. However, once the specimen was pulled taut, the load cell began to deflect indicating force borne on the NW. Despite the change in system stiffness in this state (denoted by green shaded region) no apparent change in displacement rate of the actuator was measured. In this loading regime, the load cell and relative grip displacements are linearly correlated, indicating a linear elastic response. The maximum load cell displacement at the peak of the loading corresponds to approximately 2.9 μ N, which is an engineering stress of 1.7 GPa in this NW. Inspection of the unload portion of the curve shows near symmetry, indicating the process to be entirely reversible. Most importantly, no residual deformation was detected in the relative grip displacement showing that deformation is elastic within this stress range.

The device and specimen were then cooled to a sample temperature of 144 K and subjected to a loading ramp to failure as shown in the bottom panel of Fig. 10. In contrast to the room temperature behavior, the load cell immediately responded to actuator motion, which is an indication of thermal contractions of the testing device and NW during cooling that served to remove the pre-buckled state prior to testing. At approximately 0.15 μ m of load cell deflection relative to the initial state for a total force of 6.6 μ N on the sample, the load instantaneously dropped, indicating fracture of the NW. This

event is accompanied by a slight surge of the actuator owing to a sudden change in system stiffness. Notably, the load cell did not return to its original position; rather, the fully unloaded state corresponds to an apparent negative value of displacement. This behavior indicates a pre-tension on the wire at the onset of tensile testing, again a result of thermal contraction during cooling of the MEMS device. We note that this apparent offset exceeded the pre-buckling intentionally imposed during manipulation of the NW, providing a quantitative estimate for the degree of thermal expansion and guidance for the pre-actuation necessary for a given target temperature. Future characterization at a range of temperatures will allow for more refined estimates of this pre-actuation leading to a zero-stress initial state. Most importantly, the load-free reference state provides the pre-tension quantity needed to calculate the absolute stress applied to the NW, as illustrated in the stress-strain curve at 144 K shown in Fig. 11.

B. Temperature-dependent tensile response

The tensile engineering stress-engineering strain response of Pd NWs was found to be strongly dependent on the testing temperature. Fig. 11 shows the stress-strain behavior for 3 different NWs with diameters of 46, 73, and 40 nm at testing temperatures of 144, 295, and 441 K, respectively (left, center, and right panels). For each individual NW, a room temperature load-unload test was performed prior to the test to fracture, as shown offset along the strain axis. In all cases, the load-unload response demonstrated full elastic recovery, even when subjected to stresses as high as 3 GPa. Thus, we reason that incipient plasticity immediately preceded final fracture, as evidenced in detail in earlier work.⁵⁴ Beginning with the room temperature behavior of the 73 nm NW (Fig. 11, center panel), we measured an apparent nonlinearity of the response at large strains (greater than $\sim 1\%$) followed by fracture at a strength of 3.4 GPa. The occurrence of nonlinear elastic behavior and ultrahigh strength are hallmarks of defect-free metallic nanostructures, which require stresses near the theoretical limit to initiate plastic flow. 2,32,54,73 Chen et al. previously reported on such mechanical behavior in (110) Pd NWs and attributed the nonlinear elastic response to the increasing role of anharmonicity in the interatomic potential energy with increasing strain, as well as the high strength to defect nucleation near the theoretical strength of single-crystalline Pd.54

The low-temperature (144 K) stress-strain response of a 46 nm NW was found to be markedly different from the room temperature behavior. In particular, the fracture strength of the specimen was measured to be 6.3 GPa, over 50 times higher than bulk coarse-grained Pd. Assuming a $\langle 110 \rangle$ orientation, this ultimate tensile stress corresponds to a resolved shear stress on the $\langle 111 \rangle \langle 112 \rangle$ slip system of 3.0 GPa, which is approximately $\mu/14$, where μ is the shear modulus of Pd. This result shows a pronounced dependence of strength on temperature. Moreover, no clear evidence of inelasticity is demonstrated in the stress-strain curve, suggesting that plastic deformation mechanisms are not active until the specimen reaches very high strength.

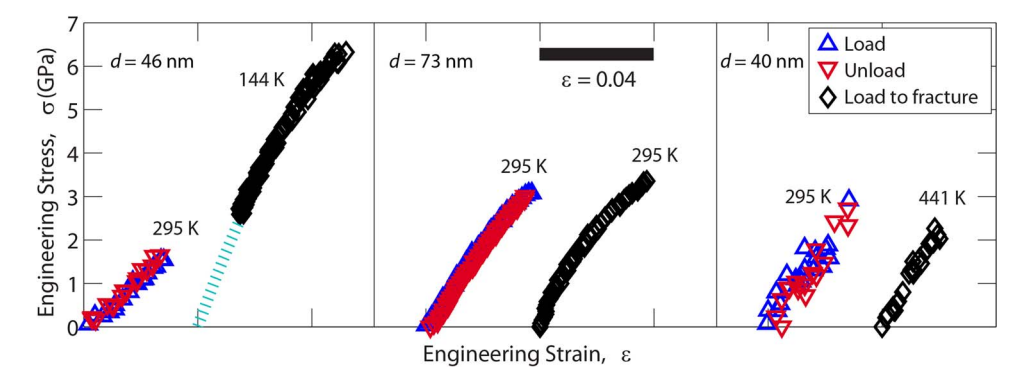


FIG. 11. Room temperature load-unload, followed by load-to-fracture stress-strain curves for 3 specimens fractured at low temperature (left panel), room temperature (middle panel), and high temperature (right panel). Load-unload experiments confirm linear elastic-behavior at room temperature. For each of the 3 wires shown, stress-strain curves are offset on strain axis for clarity.

In contrast, a wire with a similar diameter (d = 40 nm) tested at T = 441 K demonstrated lower strength relative to the lower temperature experiments, showing final fracture at 2.3 GPa. Interestingly, this NW fractured at a stress below that of the load-unload experiment performed at 295 K prior to the high-temperature experiment. Given that the load-unload response at room temperature was entirely elastic, this result unequivocally reveals a thermally activated plastic deformation mechanism. That the qualitative stress-strain behavior was similar for all testing temperatures, most notably the absence of a clear plastic flow regime, also suggests similar deformation mechanism(s). We also note that our transmission electron microscopy studies of fractured Pd NWs over a range of sizes show signatures of local plastic deformation at the fracture surfaces, indicating the activity of displacive processes. Results of this study will be published elsewhere.

In a pure single-crystalline fcc defect-free nanostructure, plastic deformation has been predicted to commence by nucleation of dislocations, which requires high stress and is expected to be thermally activated.^{28,76} This is in contrast to bulk dislocation-based plasticity mechanisms in fcc materials, such as interactions of mobile dislocations with a forest of pre-existing defects. Such defects are only weakly temperature-dependent owing primarily to the temperature dependence of μ , which sets both the obstacle strength and the friction stress of the mobile dislocation.^{77,78} Even in microscale single-crystalline fcc specimens, which have been reported to show a strong size dependence of yielding, the abundance of pre-existing dislocations that can be activated at relatively low stresses (compared with nucleation of new defect content) produces plastic activity that is athermal to first approximation. 79,80 For defect-free materials on the other hand, several researchers have estimated the atomistic processes and corresponding energy barriers associated with dislocation nucleation in a pristine crystal via molecular dynamics simulations and transition state theory, 27,81-83 in particular those of heterogeneous dislocation nucleation from a free surface. 28, 29, 76, 84 Taken as a whole, dislocation nucleation in fcc metals has been predicted to be weakly size- and strainrate dependent, yet strongly temperature-dependent.^{28,83}

For a semi-quantitative comparison of the expected yield strength difference associated with the thermal contribution to surface nucleation, we apply the model of Zhu and colleagues, 28 which is based on the combination of atomistic simulation and nudged elastic band calculations of activation barriers. In a simplified linear version of their atomistically informed theory, 85 these researchers give the reduction of stress relative to the athermal yield stress, $\Delta \sigma$, owing to thermal activation as

$$\Delta\sigma = \frac{k_B T}{\Omega} \ln \frac{k_B T N v_o}{E \dot{\epsilon} \Omega},\tag{1}$$

where Ω is the activation volume, k_BT is the thermal energy, N is the number of equivalent nucleation sites, v_o is the physical attempt frequency, E is the Young's modulus, and $\dot{\varepsilon}$ is the applied strain rate. We use values obtained from our experiments on Pd NWs to compare Eq. (1) to our measurements. Using an activation volume of $10b^3$, where b is the Burger's vector, $v_o = 3.1 \times 10^{11} \text{ s}^{-1}$, and assuming corner nucleation from our truncated rhombic cross-sectional NW shapes², Eq. (1) predicts a strength difference for $\Delta T \sim 300 \text{ K}$ of $\Delta \sigma|_{T=144 \text{ K}} = 4 \text{ GPa}$. Our experimental measurements gave a difference in strength of 4 GPa, which agrees excellently with the model for surface dislocation nucleation. Our results clearly underscore the importance of systematic experimental measurements of thermally activated plastic deformation mechanisms in single nanostructures.

We note that changes in elasticity response owing to a coupling between temperature- and size-dependent phenomena are interesting avenues of research. For instance, Chen et al. recently uncovered a large degree of anharmonicity in similar Pd NWs manifested as size-dependent linear and nonlinear elastic response.⁵⁴ As the temperature-dependence of elastic constants is tied to anharmonic response in atomic interactions, one would expect significant differences at the temperatures achieved in our setup.^{86,87} Our current measurements of Young's moduli at various temperatures, however, show substantial variation beyond the expected temperaturedependent material response due to compliance of the Ptcontaining clamping materials, as previously described. We ascribe this to the comparable stiffnesses of the clamps and the NWs,⁷² although such behavior could be exacerbated by any temperature-dependent stiffness of the organometallic clamps.

IV. CONCLUDING REMARKS

In summary, we have shown the development of a platform capable of performing temperature-dependent in situ uniaxial straining of a single nanostructure. Our system employs a compact MEMS tensile testing platform and a commercially available vacuum cryostat system, enabling a temperature range of 90–475 K. The low thermal mass of the MEMS platform offers reasonably fast attainment of a steadystate temperature regime, good temperature control, and ease of installation. By coupling this system with a standard optical microscope and digital image correlation of image sequences, we can obtain quantitative characterization of nanoscale mechanical response with adequate fidelity (e.g., for testing nanowires with sizes down to \sim 30 nm). We envision facile integration of any similar MEMS device for alternative testing modalities such as compression, bending, or indentation, as well as measurement of coupled behavior (e.g., electromechanical, thermomechanical). We demonstrated the successful application of our system to tensile testing of defect-free Pd NWs as a function of temperature, which exhibit pronounced temperature dependence of the fracture strength, a key signature of thermally activated plastic deformation mechanisms such as surface dislocation nucleation. A recent atomistically informed model of dislocation nucleation was found to agree with our measured temperature sensitivity. We expect our experimental approach to be suitable for measurements of other metallic and non-metallic quasi-1D and 2D nanostructures demonstrating unique deformation physics.⁸⁵

Several improvements to the configuration and operation of our system can be envisioned for enhanced performance and versatility. First, our temperature range could be extended by utilizing a different cryogen such as liquid helium ($T_{min} \sim$ 4 K). This larger range has the added benefit of avoiding high temperatures where nanoscale structural instabilities could appear and complicate interpretation of the measured behavior. Also, the thermal resistance between the MEMS device and the Cu cooling block could be readily reduced by using a non-ceramic electronics package, which in turn would both decrease the time required for thermal steady-state as well as minimize the temperature gradient along the conduction path. A method for direct temperature measurement of the nanostructure, such as μ -Raman spectroscopy^{88,89} or electrical resistance measurements following calibration of the temperature coefficient of resistivity, 90 would additionally reduce uncertainty arising from thermal resistance from the gripping materials. Alternatives to the Pt-containing EBID clamping material providing high stiffness and strong grips for the NWs, such as those deposited directly using shadow masking, should be pursued to enable nanoscale measurements of temperature-dependent elasticity. Finally, we foresee the use of enhanced control of the actuator motion during heating and cooling based on feedback from real-time DIC measurement, which would also facilitate transient experiments such as creep, temperature jump, etc.

ACKNOWLEDGMENTS

This research was supported by the National Science Foundation through a CAREER Award No. DMR-1056293.

We acknowledge additional support through start-up funding from the University of Pennsylvania. We thank G. Richter (Max Planck Institute for Intelligent Systems) for providing the Pd NWs and M. He and B. Piccione (University of Pennsylvania) for technical assistance and fruitful discussions. The authors also thank the support of the staff and facilities at the Penn Regional Nanotechnology Facility and the Nano/Bio Interface Center (supported by NSF DMR-0923245) at the University of Pennsylvania. This work was performed, in part, at the Center for Integrated Nanotechnologies, a U.S. Department of Energy, Office of Basic Energy Sciences user facility. Sandia National Laboratories is a multi-program laboratory managed and operated by Sandia Corporation, a wholly owned subsidiary of Lockheed Martin Corporation, for the U.S. Department of Energy's National Nuclear Security Administration under Contract No. DE-AC04-94AL85000.

- ¹Y. Zhu, Q. Qin, F. Xu, F. Fan, Y. Ding, T. Zhang, B. J. Wiley, and Z. L. Wang, Phys. Rev. B **85**, 045443 (2012).
- ²G. Richter, K. Hillerich, D. S. Gianola, R. Mönig, O. Kraft, and C. A. Volkert, Nano Lett. **9**, 3048 (2009).
- ³Y. Lu, C. Peng, Y. Ganesan, J. Y. Huang, and J. Lou, Nanotechnology 22, 355702 (2011).
- ⁴J. Y. Huang, H. Zheng, S. X. Mao, Q. Li, and G. T. Wang, Nano Lett. **11**, 1618 (2011).
- ⁵J. J. Brown, A. I. Baca, K. A. Bertness, D. A. Dikin, R. S. Ruoff, and V. M. Bright, Sens. Actuators A **166**, 177 (2011).
- ⁶H. S. Park and X. Qian, J. Phys. Chem. C **114**, 8741 (2010).
- ⁷W. Wang, Q. Yang, F. Fan, H. Xu, and Z. L. Wang, Nano Lett. 11, 1603 (2011).
- ⁸D. Li, Y. Wu, P. Kim, L. Shi, P. Yang, and A. Majumdar, Appl. Phys. Lett. 83, 2934 (2003).
- ⁹R. Chen, A. I. Hochbaum, P. Murphy, J. Moore, P. Yang, and A. Majumdar, Phys. Rev. Lett. **101**, 105501 (2008).
- ¹⁰ M. I. Ferguson, D. Keymeulen, C. Peay, K. Yee, and D. L. Li, in 2005 IEEE Aerospace Conference (IEEE, 2005), pp. 1–6.
- ¹¹K. Shcheglov, C. Evans, R. Gutierrez, and T. K. Tang, in 2000 IEEE Aerospace Conference Proceedings (Cat. No. 00TH8484) (IEEE, 2000), pp. 403–411.
- ¹²I. Chakraborty, W. Tang, D. Bame, and T. Tang, Sens. Actuators A 83, 188 (2000).
- ¹³Y. Zhu and H. D. Espinosa, Int. J. RF Microw. Comput. Eng. **14**, 317 (2004).
- ¹⁴H. Su, I. Llamas-Garro, and M. Lancaster, Electron. Lett. **42**, 1219 (2006).
- ¹⁵C. Pramanik, H. Saha, and U. Gangopadhyay, J. Micromech. Microeng. 16, 2060 (2006).
- ¹⁶K. Oyama, M. Takabayashi, Y. Takei, S. Arai, S. Takeoka, S. Ishiwata, and M. Suzuki, Lab Chip 12, 1591 (2012).
- ¹⁷A. Nisar, N. Afzulpurkar, B. Mahaisavariya, and A. Tuantranont, Sens. Actuators B 130, 917 (2008).
- ¹⁸R. Klingeler, S. Hampel, and B. Büchner, Int. J. Hyperthermia 24, 496 (2008).
- ¹⁹A. Shakouri, Annu. Rev. Mater. Res. **41**, 399 (2011).
- ²⁰G. J. Snyder and E. S. Toberer, Nat. Mater. 7, 105 (2008).
- ²¹C. K. Chan, H. Peng, G. Liu, K. McIlwrath, X. F. Zhang, R. A. Huggins, and Y. Cui, Nat. Nanotechnol. 3, 31 (2008).
- ²²J. Y. Huang, L. Zhong, C. M. Wang, J. P. Sullivan, W. Xu, L. Q. Zhang, S. X. Mao, N. S. Hudak, X. H. Liu, A. Subramanian, H. Fan, L. Qi, A. Kushima, and J. Li, Science 330, 1515 (2010).
- ²³ K. Zhao, M. Pharr, J. J. Vlassak, and Z. Suo, J. Appl. Phys. **108**, 073517 (2010).
- ²⁴S. Karim, A. G. Balogh, and W. Ensinger, Nanotechnology 17, 5954 (2006).
- ²⁵F. A. Nichols and W. W. Mullins, Trans. Metall. Soc. AIME **233**, 1840 (1965).
- ²⁶M. E. Toimil Molares, A. G. Balogh, T. W. Cornelius, R. Neumann, and C. Trautmann, Appl. Phys. Lett. 85, 5337 (2004).
- ²⁷D. H. Warner and W. A. Curtin, Acta Mater. **57**, 4267 (2009).
- ²⁸T. Zhu, J. Li, A. Samanta, A. Leach, and K. Gall, Phys. Rev. Lett. **100**, 025502 (2008).

- ²⁹S. Ryu, K. Kang, and W. Cai, Proc. Natl. Acad. Sci. U.S.A. **108**, 5174 (2011)
- ³⁰C. Peng, Y. Zhan, and J. Lou, Small 8, 1889 (2012).
- ³¹C. R. Weinberger and W. Cai, J. Mater. Chem. **22**, 3277 (2012).
- ³²A. Sedlmayr, E. Bitzek, D. S. Gianola, G. Richter, R. Mönig, and O. Kraft, Acta Mater. 60, 3985 (2012).
- ³³Y. Ge, W. Song, X. Wang, Z. Luo, W. Li, and J. Lin, Mater. Chem. Phys. 124, 25 (2010).
- ³⁴J. M. Wheeler, R. Raghavan, and J. Michler, Scr. Mater. **67**, 125 (2012).
- ³⁵ M. Zaiser, J. Schwerdtfeger, A. S. Schneider, C. P. Frick, B. G. Clark, P. A. Gruber, and E. Arzt, Philos. Mag. 88, 3861 (2008).
- ³⁶J. M. Wheeler and J. Michler, Rev. Sci. Instrum. **84**, 045103 (2013).
- ³⁷C. A. Schuh, J. K. Mason, and A. C. Lund, Nat. Mater. 4, 617 (2005).
- ³⁸ J. C. Trenkle, C. E. Packard, and C. A. Schuh, Rev. Sci. Instrum. 81, 073901 (2010).
- ³⁹ A. A. Volinsky, N. R. Moody, and W. W. Gerberich, J. Mater. Res. 19, 2650 (2011).
- ⁴⁰B. D. Beake and J. F. Smith, *Philos. Mag. A* **82**, 2179 (2002).
- ⁴¹J. M. Wheeler, P. Brodard, and J. Michler, Philos. Mag. **92**, 3128 (2012).
- ⁴²V. Gonda, K. M. B. Jansen, L. J. Ernst, J. den Toonder, and G. Q. Zhang, Microelectron. Reliab. 47, 248 (2007).
- ⁴³T. G. Nieh, C. Iwamoto, Y. Ikuhara, K. W. Lee, and Y. W. Chung, Intermetallics 12, 1183 (2004).
- ⁴⁴A. Sawant and S. Tin, Scr. Mater. **58**, 275 (2008).
- ⁴⁵H. Lee, Y. Chen, A. Claisse, and C. A. Schuh, Exp. Mech. **53**, 1201 (2013).
- ⁴⁶W. Kang and M. T. A. Saif, J. Micromech. Microeng. **21**, 105017 (2011).
- ⁴⁷P. A. Gruber, S. Olliges, E. Arzt, and R. Spolenak, J. Mater. Res. 23, 2406 (2011).
- ⁴⁸M. A. Haque and M. T. A. Saif, Thin Solid Films **484**, 364 (2005).
- ⁴⁹D. S. Gianola, A. Sedlmayr, R. Mönig, C. A. Volkert, R. C. Major, E. Cyrankowski, S. A. S. Asif, O. L. Warren, and O. Kraft, Rev. Sci. Instrum. 82, 063901 (2011).
- ⁵⁰Y. Lu, Y. Ganesan, and J. Lou, Exp. Mech. **50**, 47 (2009).
- ⁵¹J.-Y. Kim, D. Jang, and J. R. Greer, Acta Mater. **58**, 2355 (2010).
- ⁵²A. T. Jennings and J. R. Greer, *Philos. Mag.* **91**, 1108 (2011).
- ⁵³D. Kiener and A. M. Minor, Nano Lett. **11**, 3816 (2011).
- ⁵⁴L. Chen, G. Richter, J. Sullivan, and D. Gianola, Phys. Rev. Lett. 109, 125503 (2012).
- ⁵⁵G. Richter, Scr. Mater. **63**, 933 (2010).
- ⁵⁶H. H. Burke and I. P. Herman, *Phys. Rev. B* **48**, 15016 (1993).
- ⁵⁷T. R. Hart, R. L. Aggarwal, and B. Lax, Phys. Rev. B 1, 638 (1970).
- ⁵⁸Q. Qin and Y. Zhu, Appl. Phys. Lett. **102**, 013101 (2013).
- ⁵⁹R. Hickey, M. Kujath, and T. Hubbard, J. Vac. Sci. Technol. A **20**, 971 (2002).

- ⁶⁰C. Eberl, D. S. Gianola, and K. J. Hemker, Exp. Mech. **50**, 85 (2008).
- ⁶¹D. S. Gianola and C. Eberl, **JOM 61**, 24 (2009).
- ⁶²C. Eberl, R. Thompson, D. Gianola, W. J. Sharpe, and K. Hemker, Mat-LabCentral, Mathworks File Exchange Server, FileID 12413, 2006.
- ⁶³P. Flubacher, A. J. Leadbetter, and J. A. Morrison, Philos. Mag. 4, 273 (1959).
- ⁶⁴C. A. Swenson, J. Phys. Chem. Ref. Data **12**, 179 (1983).
- ⁶⁵K. G. Lyon, G. L. Salinger, C. A. Swenson, and G. K. White, J. Appl. Phys. 48, 865 (1977).
- $^{66}\mbox{V}.$ Glazov and A. Pashinkin, High Temp. $\pmb{39},\,443$ (2001).
- ⁶⁷A. Botman, J. J. L. Mulders, R. Weemaes, and S. Mentink, Nanotechnology 17, 3779 (2006)
- ⁶⁸W. F. van Dorp and C. W. Hagen, J. Appl. Phys. **104**, 081301 (2008).
- ⁶⁹W. Ding, D. a. Dikin, X. Chen, R. D. Piner, R. S. Ruoff, E. Zussman, X. Wang, and X. Li, J. Appl. Phys. **98**, 014905 (2005).
- ⁷⁰V. Friedli, I. Utke, K. Mølhave, and J. Michler, Nanotechnology 20, 385304 (2009).
- ⁷¹Q. Qin, F. Xu, Y. Cao, P. I. Ro, and Y. Zhu, Small 8, 2571 (2012).
- ⁷²K. F. Murphy, L. Y. Chen, and D. S. Gianola, Nanotechnology **24**, 235704 (2013).
- ⁷³K. E. Johanns, A. Sedlmayr, P. Sudharshan Phani, R. Mönig, O. Kraft, E. P. George, and G. M. Pharr, J. Mater. Res. 27, 508 (2011).
- ⁷⁴G. Jimenez, E. Dillon, R. Miller, F. Massicotte, S. Nesbit, and A. Craft, Scr. Mater. **59**, 870 (2008).
- ⁷⁵R. Smith and D. Otterson, J. Less Common Met. **24**, 419 (1971).
- ⁷⁶C. R. Weinberger and W. Cai, Proc. Natl. Acad. Sci. U.S.A. **105**, 14304 (2008).
- ⁷⁷ A. Iskandarov, S. Dmitriev, and Y. Umeno, *Phys. Rev. B* **84**, 224118 (2011).
- ⁷⁸M. F. Ashby, C. Gandhi, and D. M. R. Taplin, Acta Metall. **27**, 699 (1979).
- ⁷⁹A. T. Jennings, J. Li, and J. R. Greer, Acta Mater. **59**, 5627 (2011).
- ⁸⁰C. Zhou, I. J. Beyerlein, and R. Lesar, Acta Mater. **59**, 7673 (2011).
- ⁸¹G. Norman and A. Yanilkin, Phys. Solid State **53**, 1614 (2011).
- ⁸²K. Kang and W. Cai, Int. J. Plast. **26**, 1387 (2010).
- ⁸³D. E. Spearot, M. A. Tschopp, and D. L. Mcdowell, Scr. Mater. **60**, 675 (2009).
- ⁸⁴L. Nguyen, K. Baker, and D. Warner, *Phys. Rev. B* **84**, 024118 (2011).
- ⁸⁵T. Zhu and J. Li, Prog. Mater. Sci. **55**, 710 (2010).
- ⁸⁶H. Masumoto, H. Saito, and S. Kadowaki, Sci. Reports Res. Inst., Tohoku Univ. Ser. A 19, 294 (1967).
- ⁸⁷J. Rayne, Phys. Rev. **118**, 1545 (1960).
- ⁸⁸J. Lee, T. Beechem, T. L. Wright, B. A. Nelson, S. Graham, and W. P. King, J. Microelectromech. Syst. 15, 1644 (2006).
- ⁸⁹Y. Yue, G. Eres, X. Wang, and L. Guo, Appl. Phys. A **97**, 19 (2009).
- ⁹⁰C. D. S. Brites, P. P. Lima, N. J. O. Silva, A. Millán, V. S. Amaral, F. Palacio, and L. D. Carlos, Nanoscale 4, 4799 (2012).